

# Supporting Information: Symmetry Breaking-Induced N-body Electrodynamic Forces in Optical Matter Systems

John Parker<sup>1,2,\*</sup>, Spoorthi Nagasamudram<sup>1,2,\*</sup>, Curtis Peterson<sup>2,3,\*</sup>, Yanzeng Li<sup>1,4,\*†</sup>, Sina  
Soleimanikahnoj<sup>1</sup>, Stuart A. Rice<sup>1,3</sup>, and Norbert F. Scherer<sup>1,3,†</sup>

<sup>1</sup>*James Franck Institute, The University of Chicago, Chicago, IL 60637, USA*

<sup>2</sup>*Department of Physics, The University of Chicago, Chicago, IL 60637, USA*

<sup>3</sup>*Department of Chemistry, The University of Chicago, Chicago, IL 60637, USA*

<sup>4</sup>*Department of Physics, Optical Engineering, and Nanoengineering, Rose-Hulman Institute of  
Technology, Terre Haute, IN 47803, USA*

*\*These authors contributed equally*

*†Corresponding authors: liy2@rose-hulman.edu; nfschere@uchicago.edu*

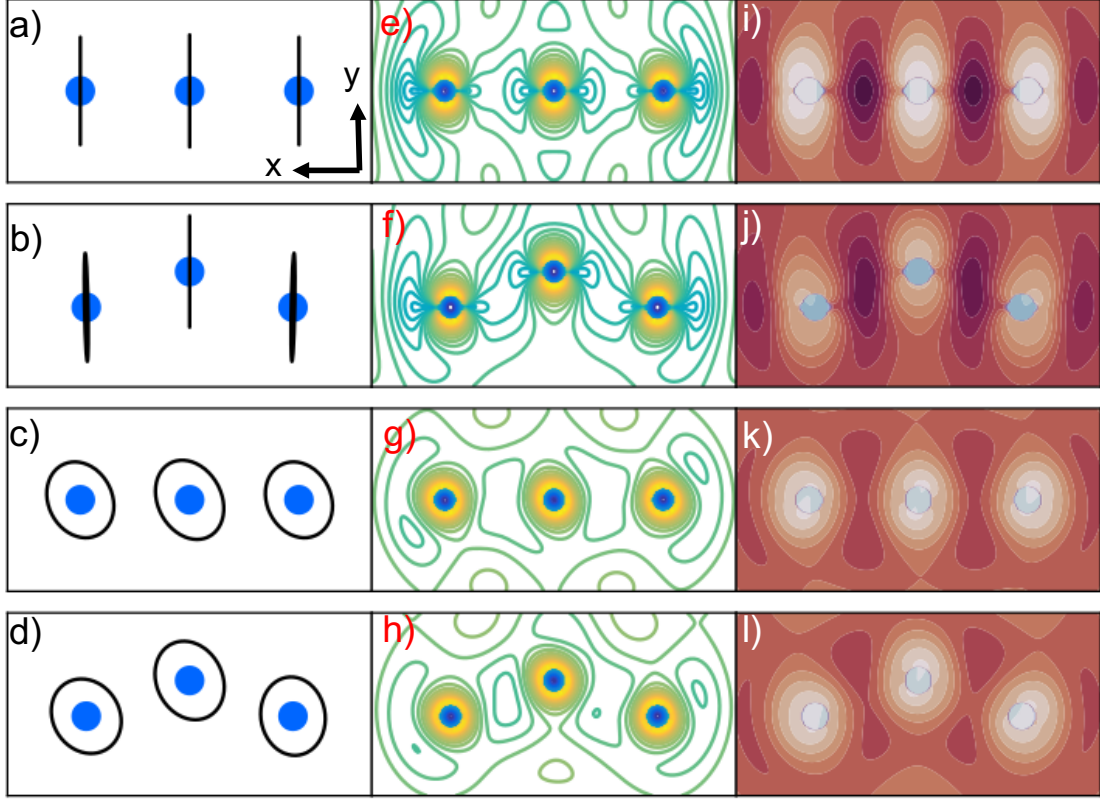
## Contents

Supplementary Note 1.	Broken electromagnetic field symmetry due to three-body coupling . . . . .	4
Supplementary Note 2.	N-body force as a function of ring radius . . . . .	6
Supplementary Note 3.	Simulations of optical ring traps . . . . .	7
Supplementary Note 4.	Scattering enhancement due to electrodynamic interactions in a filled ring . . . . .	9
Supplementary Note 5.	N-body force for elliptically polarized light . . . . .	10
Supplementary Note 6.	Experimental setup for formation and measurement of optical matter rings of nanoparticles . . . . .	12
Supplementary Note 7.	Defining and employing a collective coordinate to average random Brownian fluctuations . . . . .	14
Supplementary Note 8.	Experimental Velocity Distributions . . . . .	16
Supplementary Note 9.	Mean-squared displacement analysis of nanoparticle transport . . . . .	17
Supplementary Note 10.	Effects of Zernike polynomials on N-body forces in experiments . . . . .	20
Supplementary Note 11.	N-body force in over-filled rings and with near-field dimer perturbations . . . . .	22
Supplementary Note 12.	Stuck particles in a ring trap can impede collective motion	24
Supplementary Note 13.	Autocorrelation function (ACF) analysis of the transport	25
Supplementary Note 14.	Non-uniform experimental velocity distributions . . . . .	28
Supplementary Note 15.	Radial coordinate in a driven ring . . . . .	30

Supplementary Note 16.	Consideration of contributions to the N-body effect from nanoparticles' absorption . . . . .	31
------------------------	--	----

## Supplementary Note 1. Broken electromagnetic field symmetry due to three-body coupling

Supplementary Figure 1 complements parts of main text Figure 1. Supplementary Figure 1(a-d) shows the induced dipole for a linear trimer of polarizable nanoparticles and bent trimer illuminated by linearly polarized and circularly polarized light (plane wave). Panels (e-h) and (i-l) show the corresponding intensity and phase of the scattered light, respectively. For light linearly polarized in the  $y$  direction (i.e., vertical), we can see from Supplementary Figure 1(e-f) and (i-j) that the intensity and phase contours for a linear trimer are mirror symmetric in both the  $x$  and  $y$  directions. However, for a bent trimer, the structural symmetry is broken in the  $y$ -direction (i.e., about the  $x$ -axis) and the induced-polarization of particles (black ellipses) have differing amounts of tilt (i.e., the magnitude of the induced dipole—induced-polarization—as a function of time in one optical cycle) and therefore broken symmetry about the  $y$ -axis (vertical direction). These features are more apparent in the phase (and intensity) contours, shown in Supplementary Figure 1(f,j) vs Supplementary Figure 1(e,i). A non-reciprocal force results in the vertical direction. Note that the size of the ellipses shown is for illustration purposes. The driven displacement of conduction band electrons is smaller than and bounded by the metal (Ag) nanoparticle size.

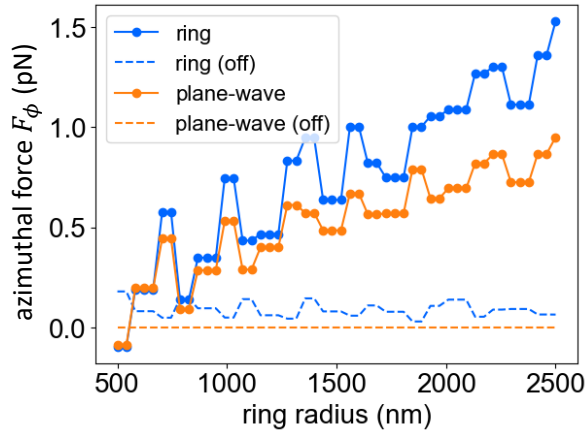


**Supplementary Figure 1: Ag nanoparticle configurations, induced dipole moments, electromagnetic field intensities and phases.** (a-d) Induced dipoles (black) in the linear and bent trimer for (a,b)  $y$ -polarized light and (c,d) RHC-polarized light. (e-h) Electromagnetic field intensity contours around the linear and bent trimer structures for (e,f)  $y$ -polarized light and (g,h) RHC-polarized light. (i,j) Phase of  $E_y$ , the  $y$ -component of the electromagnetic field for linearly polarized light along the  $y$ -direction. (k,l) Phase of  $E_x - iE_y$ , the RHC-component of the electromagnetic field for RHC-polarized incident light.

Supplementary Figure 1(c,g,k) show that for circularly polarized light, the induced polarization, intensity and phase contours for a linear trimer have (or almost have) inversion symmetry but not mirror reflection symmetry. However, Supplementary Figure 1(d,h,l) for a bent trimer shows that inversion symmetry is broken, resulting in a force along the  $x$ -axis (i.e., in the horizontal direction) whose direction ( $+x, -x$ ) is determined by the handedness of the circular polarization.

## Supplementary Note 2. N-body force as a function of ring radius

The main point of this work—that the new type of force observed for polarizable nanoparticles in a ring trap arises from the N-body electrodynamic interactions between the particles—is demonstrated by simulating a system without electrodynamic interactions amongst the particles. This is shown in Supplementary Fig. 2 for optically bound nanoparticles in an optical ring trap as well as a plane wave incident beam. The driving force is zero for the plane wave simulation without interactions. The azimuthal force is nonzero but very small for a ring trap without interactions due to spin-orbit coupling of light, which is nonzero for (tightly) focused optical beams [1–4]. By contrast, the N-body interactions dominate and determine the driving force in electrodynamics-Langevin dynamics (EDLD) simulations when the inter-particle electrodynamic interactions are included. As the radius of the ring is increased the number of particles that can be accommodated along the expanding circumference of the ring increases discretely. Additionally, the interparticle separation, which also affects the N-body force  $F_\phi(R, N)$  as demonstrated in Eq. 1 of the main text, varies periodically due to alternating compression and relaxation (dilation) of interparticle separation as the radius,  $R$ , and circumference are increased and also the particle number,  $N$ . Discrete jumps in the force are related to obtaining more ideal interparticle separations for certain ratios of ring trap circumference to the number of nanoparticle constituents. The upward trend in  $F_\phi(R, N)$  is an additive effect of increasing particle number.



**Supplementary Figure 2: Azimuthal force  $F_\phi(R, N)$  in a filled ring as the ring radius and number of Ag nanoparticles it contains increase.** When pairwise and N-body interactions are disabled (turned off; dashed), the azimuthal force in the plane-wave (orange dashed) vanishes. For the ring, there exists a small driving force (blue dashed) without interactions due to spin-orbit coupling. The driving force increases significantly when interactions are enabled (solid).

### Supplementary Note 3. Simulations of optical ring traps

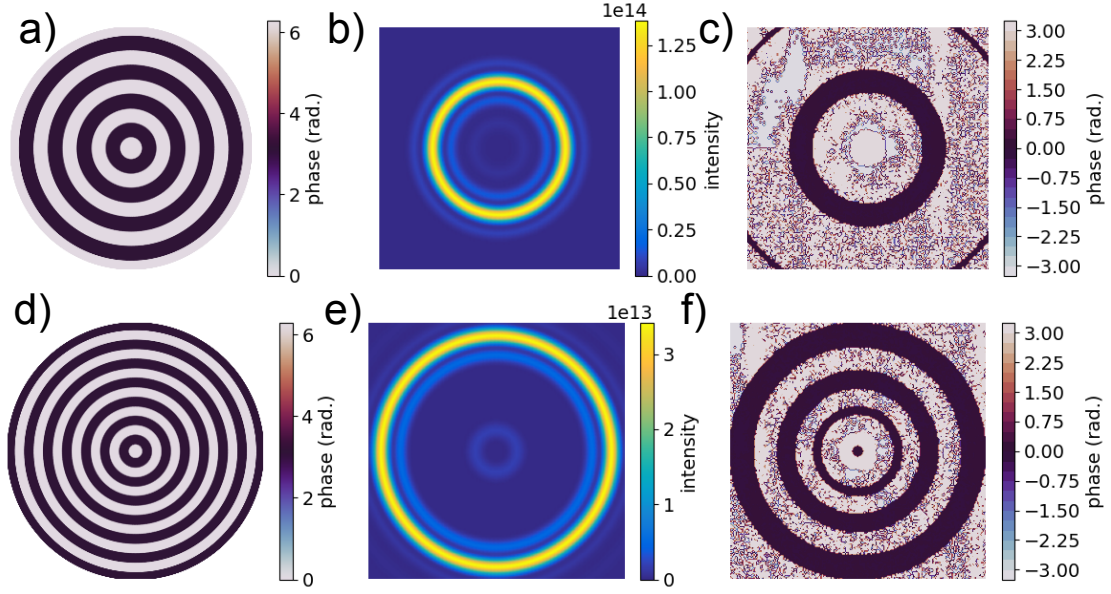
The optical ring trap in experiment can be simulated using phase-shaping holography. For a ring trap with radius  $R$  and winding number  $l$ , the field in the conjugate focal plane is given by [5, 6]:

$$\psi(\boldsymbol{\rho}) = \psi_0 J_l(C, \rho) e^{il\theta} \quad (1)$$

where  $\boldsymbol{\rho} = (\rho, \theta)$  is the polar coordinate in 2 dimensions,  $\psi_0$  represents the amplitude profile of the incident Gaussian beam,  $J_l$  is the  $l$ -th order Bessel function of the first kind and  $C$  is determined by the radius of the ring, wavelength of the coherent laser light and the focal length of the optical system. We generate this optical field in simulation by mimicing a phase-only spatial light modulator (SLM). The phase function associated with the ring trap is given by:

$$\phi(\boldsymbol{\rho}) = \{l\theta + \pi H(-J_l(C, \rho))\} \bmod 2\pi. \quad (2)$$

where  $H(x)$  is the Heaviside function. The first term ( $l\theta$ ) controls the azimuthal phase profile and the second term controls the radial amplitude profile of a ring with a fixed radius  $R$  that does not vary with  $l$ . In our simulations, Supplementary Eq. 2 was used with  $l = 0$  to generate a ring trap with no azimuthal phase gradient. Supplementary Figure 3(a,d) shows the phase profile on the SLM, Supplementary Fig. 3(b,e) the focal field intensity and Supplementary Fig. 3(c,f) phase profiles for rings of radius  $2.5 \mu m$  (top row) and  $4.05 \mu m$  (bottom row). As expected, the phase functions on the simulated SLM and in the focal field are independent of  $\theta$ . High-intensity regions in Supplementary Figure 3(b) and (e) are where the nanoparticles would be located in the ring trap.

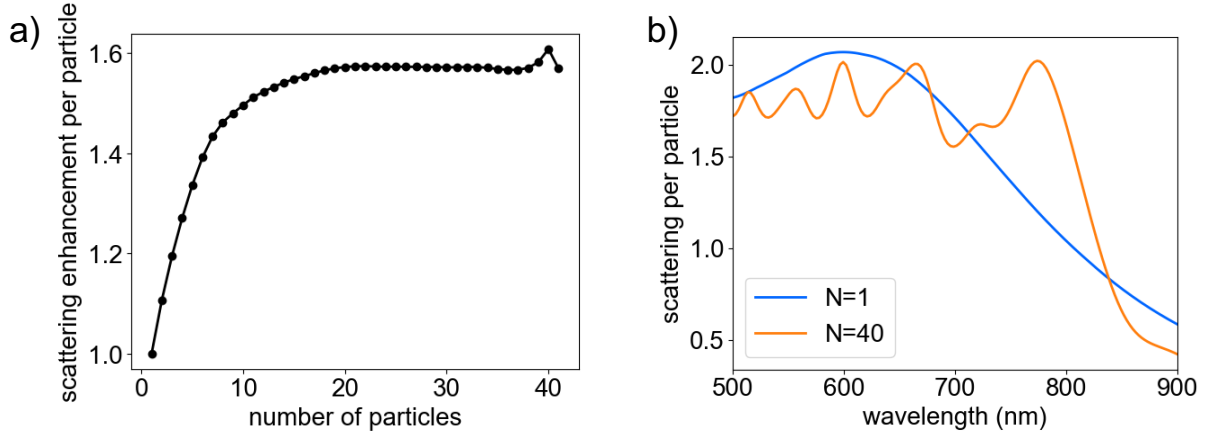


**Supplementary Figure 3: SLM phase functions, focal plane intensities and phase profiles used in simulations.** (a) Phase on the SLM for an optical ring of radius  $2.5\,\mu\text{m}$ . (b) Focal field intensity for the given SLM. (c) Focal field phase for the given SLM. (d-f) Analogous plots for an optical ring of radius  $4.05\,\mu\text{m}$ .



## Supplementary Note 4. Scattering enhancement due to electrodynamic interactions in a filled ring

Supplementary Figure 4(a) shows the Generalized Multiparticle Mie Theory (GMMT)-simulated enhancement of per particle scattering as a function of the number of particles in an optical matter ring constituted of 150 nm dia. Ag particles. The scattering per particle is enhanced for two or more particles due to electrodynamic interactions. N-body interactions only begin at 3 particles. Supplementary Figure 4(b) shows the scattering spectrum for a ring of 40 Ag particles as well as a single Ag particle illuminated by a circularly polarized plane wave. The scattering spectrum in Supplementary Fig. 4(b) shows an enhancement of scattering at the wavelength of the trapping laser ( $\lambda = 800\text{nm}$ ) that is due to collective induced-polarization(s) [7] and N-body interactions. The scattering enhancement in Supplementary Fig. 4(a) saturates because of diminishing interaction strength with increasing cord lengths and also the decreasing combinatorial for larger N-body terms.



**Supplementary Figure 4: Simulated per particle scattering enhancements.** (a) The normalized scattering enhancement per particle,  $C_{\text{scat}}(N)/C_{\text{scat}}(1)$ , as the optical ring is progressively filled with particles. (b) Per particle scattering for a single 150 nm Ag dia. particle (blue) and a ring of N=40 150 nm Ag particles (orange) illuminated by a circularly polarized plane-wave.

## Supplementary Note 5. N-body force for elliptically polarized light

Supplementary Figure 5 shows the dependence of the N-body force on the polarization state of the coherent (trapping) beam of light. The figure shows the N-body driving force (normalized so that its range is from -1 to 1) as a function of the ellipticity,  $\beta$ , of the polarization of the trapping beam of light, given by  $[1, i\beta]$ . When  $\beta = 1$ , the beam is right-handed circularly polarized, and the beam is left-handed circularly polarized when  $\beta = -1$ . When  $\beta = 0$ , the beam is linearly polarized. For all other values of  $\beta$  between -1 and 1, the beam is elliptically polarized. The red dots (curve) in Supplementary Fig. 5 represent the values of the N-body driving force and the black ellipses depict the polarization state of the beam as  $\beta$  is changed along the x-axis.

The net inter-particle force on the three-particle system in the  $x_\xi$  direction for an elliptically polarized incident field  $[1, i\beta, 0]$  is

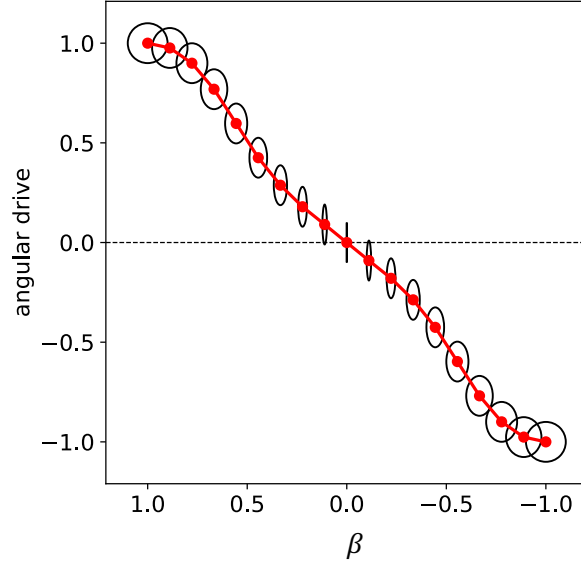
$$\langle F_{x_\xi^L} \rangle + \langle F_{x_\xi^C} \rangle + \langle F_{x_\xi^R} \rangle = \text{Re} \left[ (H_{xx} + \beta^2 H_{yy}) + i\beta (H_{xy} - H_{yx}) \right]. \quad (3)$$

where  $\overline{\overline{\mathbf{H}}}_{x_\xi}$  is given by:

$$\overline{\overline{\mathbf{H}}}_{x_\xi} = \frac{|\alpha|^2}{2} \left( \sum_i \sum_{j \neq i} \partial_{x_\xi} (\overline{\overline{\mathbf{G}}}_{ij}) + \sum_i \sum_{j \neq i} \sum_{k \neq i, j} \alpha^* \overline{\overline{\mathbf{G}}}_{ij}^* \partial_{x_\xi} (\overline{\overline{\mathbf{G}}}_{ik}) + \alpha \partial_{x_\xi} (\overline{\overline{\mathbf{G}}}_{ij}) \overline{\overline{\mathbf{G}}}_{ik} \right) + \mathcal{O}(\alpha^4), \quad (4)$$

which is similar to Eq. 2 in the main text and the same as Eq. 7 in the Method section.

For small values of ellipticity ( $|\beta| \ll 1$ ) the second term in on the righthand side of Supplementary Eq. 3 dominates and the force varies almost linearly with the ellipticity of the light. This is in agreement with the results shown in Supplementary Figure 5.



**Supplementary Figure 5: N-body Force for Varying Elliptical Polarization.** Angular drive force (red points) normalized to range from -1 to 1, of a filled optical ring trap for different elliptical polarizations of light ( $\beta$ ). The polarization states are depicted as ellipses (black) around the points for visualization, ranging from RHC (upper left) to linear to LHC (lower right). Simulations are for 150nm dia. Ag nanoparticles.

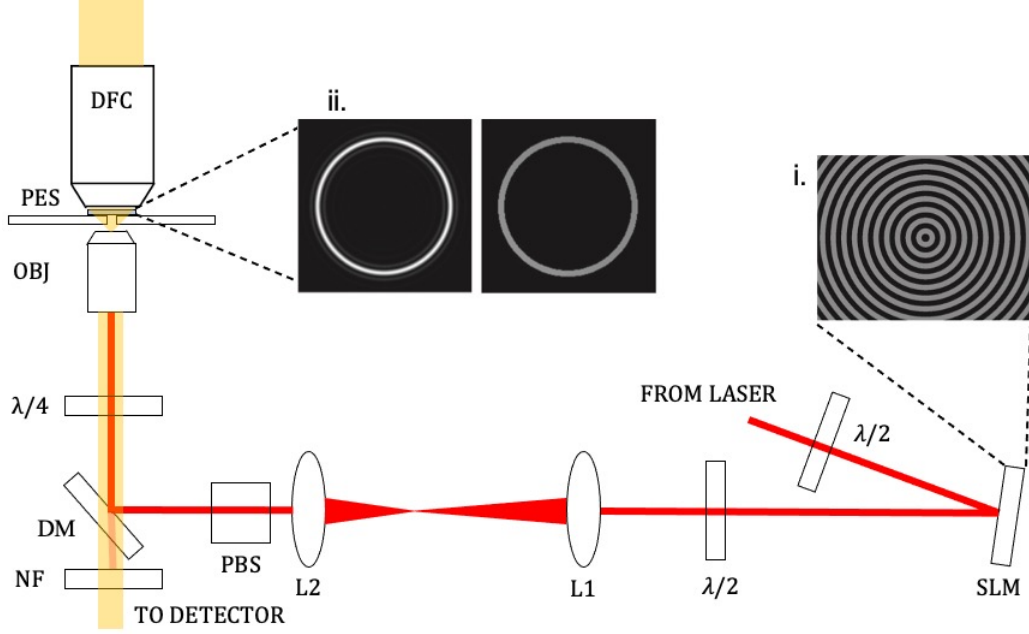
In experiment, we were only able to explore this parameter space for ellipticities of 1, 0 and  $-1$  because of practical difficulties with obtaining a fully filled ring of particles for different polarization states. The challenge mainly stemmed from optical aberrations introduced by rotating the quarter wave plate to achieve different polarization states. These results are shown in Supplementary Fig. 11.

## Supplementary Note 6. Experimental setup for formation and measurement of optical matter rings of nanoparticles

A schematic of the experimental setup is shown in Supplementary Figure 6. Our experiments were conducted with a single-beam optical tweezers setup in an inverted microscope. The experimental setup has been described previously [6, 8, 9]. A CW Ti-Sapphire laser (Spectra Physics S3900) pumped by a CW 532 nm laser (Spectra Physics Millennia Vs) is used to generate a linearly polarized Gaussian beam ( $\lambda = 770$  nm) that is incident on a phase-only spatial light modulator (SLM) (Meadowlark Optics). A half wave plate is placed before the SLM to convert the polarization to p-polarized (vertical in lab frame), which is optimal for the SLM. The SLM modifies the incident Gaussian beam according to the desired phase function for a ring trap shown in Supplementary Fig. 3, which is relayed through a 1 to 0.75 telescope, into an inverted microscope (Nikon Eclipse Ti). A half-wave plate and a polarizing beam splitter after the SLM convert the polarization of the beam back to s-polarized (horizontal in lab frame). The beam is reflected by a dichroic mirror and passes through a quarter wave plate that converts the polarization of light from linear to circular. The quarter wave plate is mounted on a piezoelectric rotation stage that could rotate at a maximum speed of  $430^\circ$  per second to enable fast switching between polarization states. The beam is then incident at the back aperture of a 60x water immersion microscope objective (Nikon 60x Plan Apo IR, NA=1.27) with an additional 1.5x magnifier inside the microscope, making the total magnification 90x. The total power measured before the microscope is 300mW. Nanoparticles (NPs) were illuminated with a high NA dark field condenser (Nikon, NA=1.25-1.43, oil immersion), and the scattered light collected by the microscope objective was imaged onto a sCMOS array detector (Andor Neo).

A 3D closed-loop piezoelectric translational stage (Mad City Labs) was used to adjust the 2D position of the sample and allows fine tuning of the imaging plane. Ring traps with  $4.1\mu\text{m}$  and  $6.2\mu\text{m}$  radii were used in the experiments. The desired intensity (left) and phase (right) profile of the ring trap is shown as an inset(Supplementary Figure 6(ii)). The phase mask used on the SLM is shown as an inset as Supplementary Figure 65(i). The zeroth-order reflection from the SLM causes the ring trap in experiment to have a Gaussian spot in the center of the ring. Even though particles occasionally get trapped in the center, they do not have an effect on the particles situated on the ring as they are

sufficiently far away and have negligible electrodynamic interactions. The focus of the optical trapping beam was adjusted independently from the imaging focus by applying a  $Z_2^0$  (Defocus) Zernike polynomial phase function on the SLM. The optical defocus resulted in tight confinement of nanoparticles in the radial direction. In addition, optical aberrations of the trap were also corrected by applying small values of the  $Z_2^2$  (Vertical astigmatism),  $Z_2^{-2}$  (Oblique astigmatism) and  $Z_3^{-3}$  (Vertical trefoil) Zernike polynomials. The values of these corrective polynomial functions were determined empirically.



**Supplementary Figure 6: Optical trapping setup for formation of ring traps.** Laser (not shown) is a CW Ti:Sapphire laser.  $\lambda/2$ : Half-wave plate, SLM: Spatial light modulator, L1: Lens 1 ( $f_1 = 100\text{cm}$ ), L2: Lens 2 ( $f_2 = 75\text{cm}$ ), DM: Dichroic mirror, NF: Notch filter,  $\lambda/4$ : Quarter wave-plate, OBJ: 60x water objective (NA 1.27), PES: Piezoelectric translation stage, DFC: Dark-field condenser with tan colors indicating the illumination and dark-field microscopy beam paths, Inset i: The phase mask applied on the SLM to create a ring trap, respectively. Inset ii: Calculated intensity (left) and phase (right) profiles at the focus of the objective.

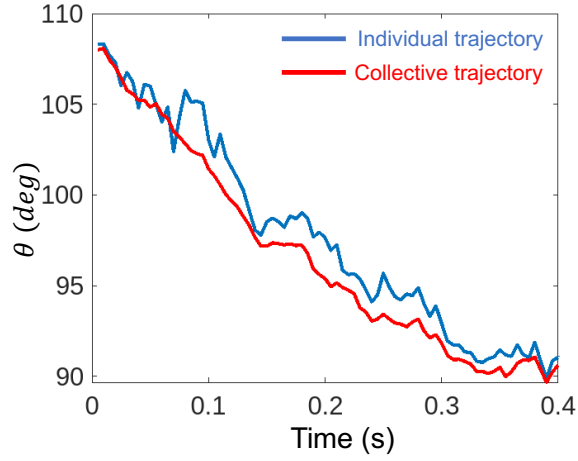
## Supplementary Note 7. Defining and employing a collective coordinate to average random Brownian fluctuations

Since experiments were performed at room temperature in aqueous solution, the nanoparticles in the ring trap experience Brownian diffusive forces and fluctuations as a result of thermal energy of the bath. The fluctuations of individual nanoparticles in the ring make it challenging to analyze the driven transport of the ring of nanoparticles. To overcome this challenge we devised an angular coordinate, termed the collective coordinate, that is obtained by cumulatively averaging the angular displacements of individual nanoparticles  $\theta_n(\cdot)$  from one frame (image) to another in darkfield microscopy videos:

$$\theta_{collective}^i = \theta_{collective}^{i-1} + \frac{1}{N} \sum_{n=1}^N (\theta_n(i+1) - \theta_n(i)) \quad (5)$$

where  $i$  is the frame number,  $n$  is the index of the trajectory, and  $N$  is the total number of trajectories (hence nanoparticles) present between frames  $i$  and  $i+1$ .

The averaging of individual nanoparticle displacements reduces the noise associated with random thermal fluctuations of the individual nanoparticles' motion that dominates their short timescale motion. Supplementary Figure 7 shows a trajectory of the angular coordinate of an individual nanoparticle in the ring trap as a function of time. Supplementary Figure 7 also shows the corresponding trajectory of the collective angular coordinate of the ring as a function of time, calculated using Supplementary Eq. 5. The trajectory of the collective coordinate is much smoother than that of the individual nanoparticle. We showed some of our results using the collective trajectories (such as in main text Fig. 2(g)), but also show some experimental velocity distributions using individual nanoparticle trajectories not the collective coordinate (such as in main text Fig. 3(d)). These different representations do not change the fundamental interpretation of our results.

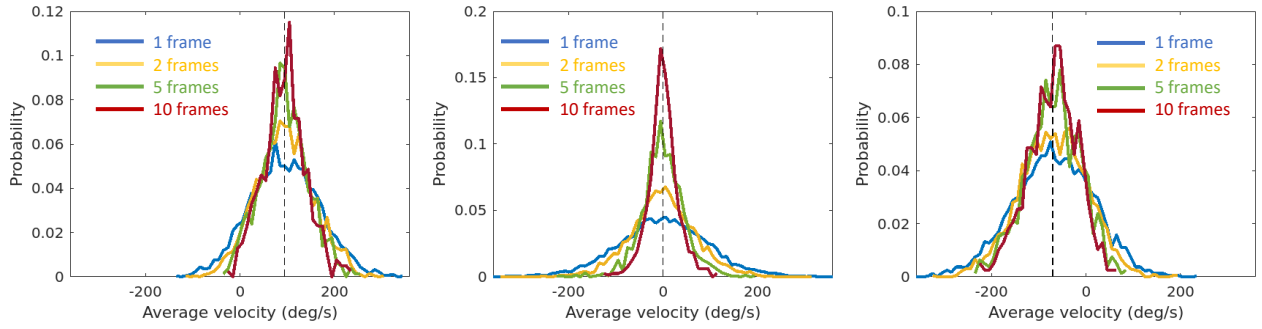


**Supplementary Figure 7: Comparison of an individual nanoparticle trajectory and the associated collective coordinate trajectory.** Trajectory of the angular coordinate of an individual nanoparticle in the experimental ring trap (blue) and the corresponding trajectory of the collective angular coordinate of all the Ag nanoparticles in the ring (red). Dark-field microscopy videos were recorded at 200 frames per second rate.

## Supplementary Note 8. Experimental Velocity Distributions

Supplementary Figure 8(a-c) shows the distribution of velocities, calculated from the collective coordinate, from experiments for different lag times  $\tau = 5\text{ms}$ ,  $10\text{ms}$ ,  $25\text{ms}$  and  $50\text{ms}$  for RHC, linear and LHC polarized light, respectively. The lag time is the time window (in frames of the video(s)) between which angular velocities are calculated. Image data are collected at 200 frames per second. For example, for a lag time of  $\tau = 5\text{ms}$  or 1 frame, the angular velocity is calculated as  $[\theta(\tau + 0.5\text{ms}) - \theta(\tau)]/5\text{ms}$ . For RHC light (Supplementary Figure 8(a)), the mean velocity is positive (counter-clockwise). For linear polarization (Supplementary Figure 8(b)), the average velocity is nearly zero for all lag times. For LHC light (Supplementary Figure 8(c)), the mean velocity is negative for all lag times.

It is important to note that the means of each set of distributions are the same indicating no lag time dependence. By contrast, the distributions narrow (by differing amounts) with lag time. The constant means indicate that the motion behaves with a constant behavior; i.e., driven superdiffusive or Brownian random. The narrowing of the distributions reflects the greater averaging of random fluctuations with increasing lag times.



**Supplementary Figure 8: Experimental velocity distributions.** Experimental velocity distributions for: (a) RHC, (b) linear, and (c) LHC polarized light for different lag times of  $\tau = 5\text{ms}$  (1 frame),  $10\text{ms}$  (2 frames),  $25\text{ms}$  (5 frames) and  $50\text{ms}$  (10 frames). Note that image data are collected at 200 frames per second. (a,c) are for a filled ring trap of radius  $6.2\mu\text{m}$  with  $N=65$  Ag nanoparticles and (b) is for a  $4.1\mu\text{m}$  radius ring trap with  $N=44$  nanoparticles. The dashed vertical line represents the means of the distributions for all lag times.



## Supplementary Note 9. Mean-squared displacement analysis of nanoparticle transport

Mean-Squared Displacement (MSD) analysis of the transport behavior provides further corroboration that the rotational motion of the nanoparticles is a collective phenomenon occurring from N-body interactions between particles in the ring. The MSD of the angular motion of each nanoparticle in the ring trap,  $\theta_n(t)$ , is calculated as:

$$\theta_{MSD}(t, \tau) = \frac{1}{N} \sum_{n=1}^N \langle |\theta_n(t) - \theta_n(t - \tau)|^2 \rangle_t = 2dD\tau^\alpha \quad (6)$$

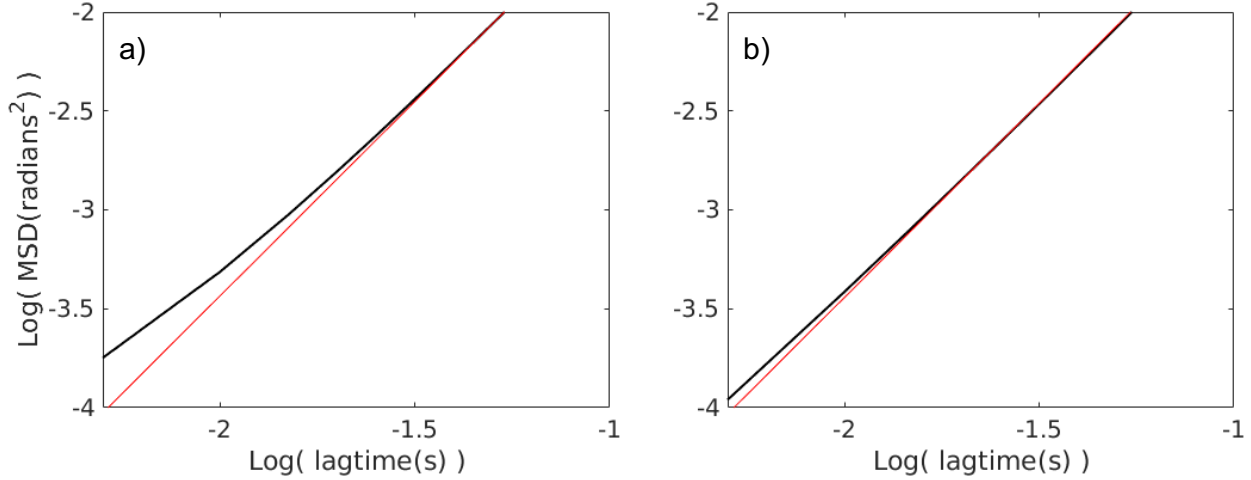
where  $d$  is the spatial dimension,  $D$  is the diffusion coefficient,  $t$  is the time in frames (in 5 msec increments),  $\tau$  is the lag time for which the MSD is calculated,  $n$  is the index of the trajectory, and  $N$  is the total number of trajectories in a given lag time. Note the averaging is done twice; once over all the frames,  $t$ , and second over all the individual trajectories of nanoparticles,  $n$ , for a given lag time. The parameter  $\alpha$  represents the transport exponent determined by the slope of the logarithm of the MSD plotted against the logarithm of the lag time, which indicates the behavior of the transport:  $\alpha = 2$  indicates driven (ballistic) motion with constant velocity,  $\alpha = 1$  indicates diffusive motion, and  $\alpha < 1$  indicates sub-diffusive (e.g., confined) motion.

Fast fluctuations in the individual particle positions are manifest in the MSD at small lag times, but these local fluctuations (random Brownian motion) average out at large lag times, so that the driven motion, which is the collective behavior of the ring of particles, dominates. This change of transport behavior — from random to driven motion — is clearly observed in Supplementary Figure 9(a). The slope of the MSD at small lag times,  $\alpha \approx 1$ , deviates from that at large lag times  $\alpha \approx 2$ .

Since rapid random motions of individual nanoparticles obscure the collective motion in the experiment (at small lag times), we devised a mechanical, collective angular coordinate of the ring of nanoparticles' motion by cumulatively averaging the angular displacements of trajectories from one image (video frame) to another (see section S7). The MSD using the collective coordinate is calculated as:

$$\theta_{MSD}(t, \tau) = \langle |\theta_{collective}(t) - \theta_{collective}(t - \tau)|^2 \rangle_t = 2dD\tau^\alpha \quad (7)$$

Note that the averaging here refers to averaging over the number of frames,  $t$ , only. We use the MSD analysis and show in Supplementary Figure 9(b) that the fast (short timescale) fluctuations are essentially removed using the collective angular coordinate, to reveal the persistent driven motion of the ring at short lag times. The slope of the MSD for the collective coordinate results at shorter lag times almost agrees with that at large lag times showing that the fast random motion (diffusive transport) has been averaged out by the collective coordinate.

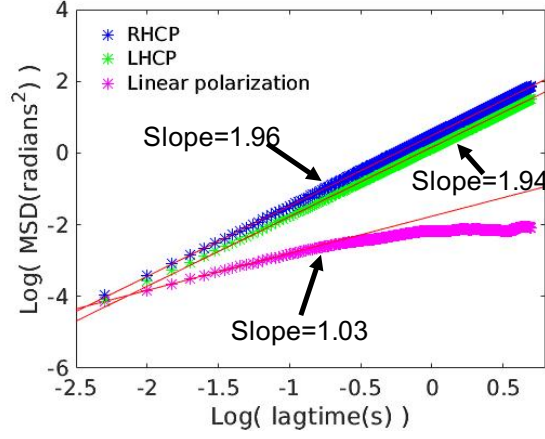


**Supplementary Figure 9: Experimental angular motion MSD analysis.** (a) The angular log MSD (black), calculated from single particle trajectories, as a function of log lag time for a ring of nanoparticles. (b) The angular log MSD calculated using the corresponding collective coordinate, as a function of log lag time. Note the red line is a linear fit to the log-log plots on long time scales ( $\log(\tau) > -1.5$ ) and has a slope  $\alpha \approx 2$ .

The MSD analysis of the collective coordinate as a function of the lag time,  $\tau$ , allows characterizing the transport:  $MSD \propto \tau^\alpha$ ,  $\alpha = 2$  indicates driven (ballistic) motion with constant velocity, while  $\alpha = 1$  indicates diffusive motion, and  $\alpha < 1$  indicates sub-diffusive (e.g., confined) motion. Since the measured slope at long lag times for both cases in Supplementary Figure 9 is nearly equal to 2, the MSD demonstrates the driven motion of the ring of nanoparticles driven by the N-body force.

The angular MSDs of the collective coordinate for LHC, RHC and linearly polarized light are shown on a log-log plot in Supplementary Figure 10. The slopes of the lines represent the transport exponent,  $\alpha$ . In the case of both LHC and RHC polarized light,  $\alpha$  is essentially 2, implying (almost) purely driven motion. When the power of the trapping beam is reduced, the ring of nanoparticles exhibits super-diffusive behaviour (i.e.  $1 < \alpha < 2$ ) because the inhomogeneous frictional drag (of nanoparticles with the nearby glass surface) becomes more significant. In the case of linearly polarized light, the

motion is diffusive at small lag times ( $\alpha \approx 1$ ) and becomes confined ( $\alpha \ll 1$ ) at larger lag times as the ring of nanoparticles is not rotating for  $\tau > 1s$ .



**Supplementary Figure 10: Mean-squared displacement analysis for different polarizations of light.** The angular mean-squared displacement (MSD) of the collective coordinate as a function of lag time for LHC, RHC and linearly polarized light. The symbols are the calculated log (MSD) values at each log (lag time), while the straight lines are fits to the MSD data at early lag times i.e., up to  $\log(\text{lag time}) = -1$  or 100 ms. The slopes of the fits, which give the values of  $\alpha$ , are shown.

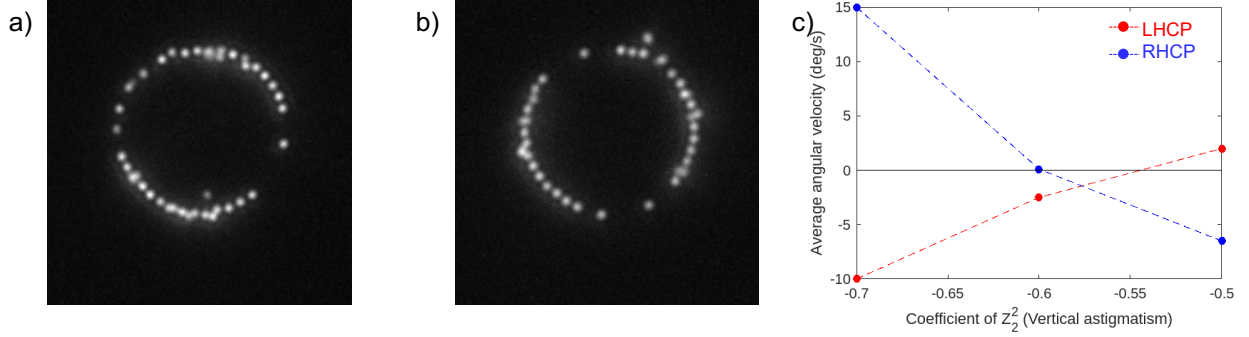
## Supplementary Note 10. Effects of Zernike polynomials on N-body forces in experiments

We took great care to establish that the experimental optical ring trap was devoid of aberrations (e.g., astigmatism and trefoil) and angular phase gradients. We observed that optical aberrations could lead to uncharacterized driven motion. One of the most important of these control studies and procedures was the observation of symmetric reversal of the angular velocity of the ring of nanoparticles when switching from RHC to LHC trapping laser light in a single experiment (i.e., with the identical particles and beam conditions).

We systematically characterized the alteration of the optical (ring) beam from the uniform spatial phase condition by introducing phase functions and aberrations through Zernike polynomials. Although these phase functions can be used to correct optical aberrations, they can also introduce non-ideal intensity and phase profiles to the ring trap that impact the motion of the ring of trapped nanoparticles. For a particular optical alignment in experiment we determined that a value of -0.6 for the coefficient of the  $Z_2^2$  (vertical astigmatism) Zernike polynomial phase function corrected for vertical astigmatism that existed in the optical system. The presence of vertical astigmatism in the experiment can be detected by looking at the reflection of the optical ring trap from the nearby glass cover slip surface. A ring trap with vertical astigmatism appears to have two high-intensity lobes along either the vertical (positive vertical astigmatism) or horizontal (negative vertical astigmatism) axis of the ring trap. Supplementary Figure 11(a,b) shows that the nanoparticles in such an aberrated ring trap tend to concentrate in these high-intensity regions or lobes and the configuration of nanoparticles does not look uniform.

Supplementary Figure 11(c) shows that when there is no vertical astigmatism in the ring trap (eliminated by applying coefficient of  $Z_2^2 = -0.6$ ), the direction of rotation is counterclockwise (clockwise) for RHC (LHC) handedness of circular polarization of light. The direction of angular motion changes from counterclockwise (clockwise) to clockwise (counterclockwise) for the RHC (LHC) handedness of circular polarization when the vertical astigmatism of the ring trap is changed from net negative (-0.7) to net positive (-0.5). While  $Z_2^2$  itself does not have a handedness in its phase profile, we observed that if the beam is incident on the objective at a small angle from normal then an angular phase gradient is created that drives the particles in the ring trap. We could eliminate this small beam tilt using piezo-tunable mirror mounts to fine tune the position and angle of the beam incident on the objective.

We did not observe the N-body rotation change direction as the  $Z_2^2$  coefficient was changed from -0.7 to -0.5 once the beam tilt was corrected. We have not simulated the N-body effect in a non-uniform ring trap as this would require exploring a extremely large parameter space of Zernike coefficients and values.

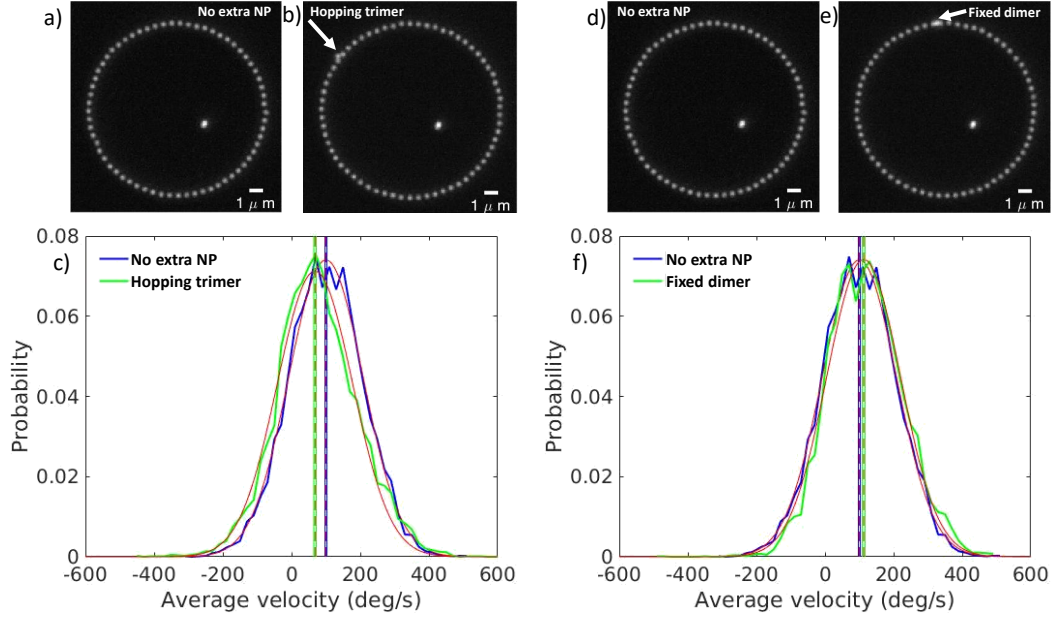


**Supplementary Figure 11: Effect of Zernike Polynomials on N-body Force.** (a) Darkfield microscopy image of 150 nm dia. Ag nanoparticles in a ring trap with positive vertical astigmatism (i.e.,  $Z_2^2 = -0.7$ ). The Ag nanoparticles are concentrated in the lobes along the top and bottom of the ring trap and fewer nanoparticles along the left and right sides. (b) Darkfield microscopy image of 150 nm dia. Ag nanoparticles in a ring trap with negative vertical astigmatism (i.e.,  $Z_2^2 = -0.5$ ). The Ag nanoparticles are concentrated along the left and right sides of the ring trap with fewer nanoparticles at the top and bottom. (c) Average angular velocity of the ring (calculated using individual nanoparticle trajectories not the collective coordinate) as a function of the Zernike coefficient  $Z_2^2$ . The phase function associated with  $Z_2^2$  is systematically added to the total phase function on the SLM. In our case, a value of -0.6 gives a ring trap with no vertical astigmatism. Values of  $Z_2^2$  greater than or less than -0.6 create a ring trap with a negative and positive vertical astigmatism, respectively.

## Supplementary Note 11. N-body force in over-filled rings and with near-field dimer perturbations

The analysis presented in the main text makes clear that structural details (i.e., interparticle separations) of the nanoparticles in the ring impact the N-body force. Supplementary Figure 12(a-f) shows two examples of an "extra" Ag nanoparticle added to an already "filled" ring. By "filled" we mean when the inter-particle spacing in the ring achieves the maximal angular drive force. In Supplementary Fig. 12(b), the extra Ag nanoparticle is "hopping" from between one pair Ag nanoparticles in the ring to the next pair while remaining outside the ring forming a local trimer. In Supplementary Fig. 12(e), the extra nanoparticle "fixes" itself to one of the nanoparticles in the ring, forming a near-field dimer [10], and rotates along with the ring. In both cases, the extra nanoparticle causes an electrodynamic perturbation to the filled ring condition.

Supplementary Figure 12(c) shows that the average speed of rotation (for lag time=5 ms; calculated using individual nanoparticle trajectories not the collective coordinate) is significantly reduced with respect to the 95% confidence interval of the mean when the extra hopping nanoparticle is added. Supplementary Figure 12(f) shows that the rotation speed (for lag time=5 ms; calculated using individual nanoparticle trajectories not the collective coordinate) is slightly enhanced with respect to the 95% confidence interval of the mean when an extra nanoparticle is added as a near-field dimer. These examples of (extra) nanoparticle perturbations in Supplementary Fig. 12, cause the structure and hence the N-body electrodynamic forces of the nanoparticles in the ring to change. The hopping particle appears to increase frictional drag and/or has a destructive electrodynamic effect, while the near-field dimer enhances the electrodynamic interactions and force.

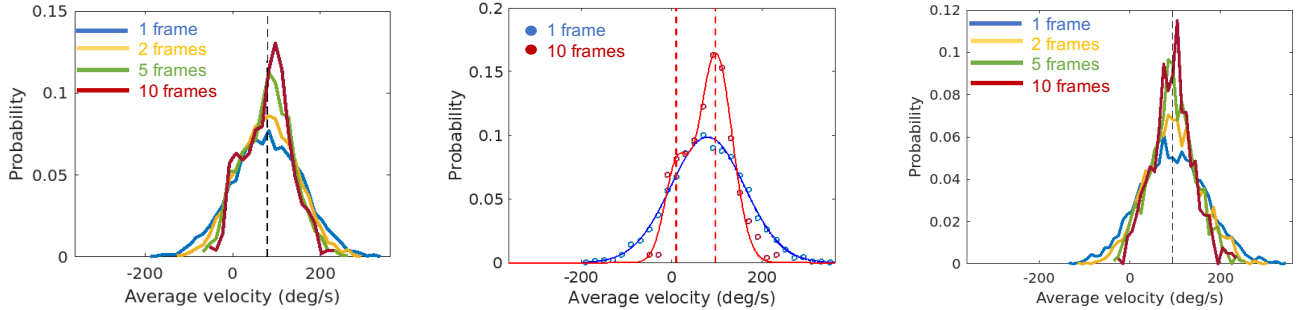


**Supplementary Figure 12: Nanoparticle perturbations to the optimally filled ring motion.**

(a) Darkfield microscopy image of a ( $R=6.2 \mu\text{m}$  radius) ring of 150 nm dia. Ag nanoparticles ( $N=65$ ) with no extra particle. (b) Darkfield microscopy image of a ring of 150 nm dia. Ag nanoparticles ( $R=6.2 \mu\text{m}$ ,  $N=66$ ) with a "hopping" dimer. The white spot inside the ring is a single Ag nanoparticle stuck to the glass coverslip. (c) Distribution of angular velocities (lag time=5 ms; calculated using individual nanoparticle trajectories not the collective coordinate) for the filled ring trap with no dimers (blue) and a filled ring trap with a particle hopping on the outside of the ring of nanoparticles (green). Solid red curves are the Gaussian fits to the distributions. Colored vertical dashed lines are the means of the fits and the thickness of the colored vertical solid lines are the 95% confidence intervals of the means. (d) Darkfield microscopy image of a ring of 150 nm dia. Ag nanoparticles ( $R=6.2 \mu\text{m}$ ,  $N=65$ ) with no extra nanoparticle. (e) Darkfield microscopy image of a ring of 150 nm dia. Ag nanoparticles ( $R=6.2 \mu\text{m}$ ,  $N=66$ ) with a "fixed" dimer. (f) Distribution of angular velocities (lag time=5 ms; calculated using individual nanoparticle trajectories not the collective coordinate) for the filled ring with no dimers (blue) and a filled ring with a dimer formed from two particles fused together (green). Solid red curves are the Gaussian fits to the distributions. Colored vertical dashed lines are the means of the fits and the thickness of the colored vertical, solid lines are the 95% confidence intervals of the means.

## Supplementary Note 12. Stuck particles in a ring trap can impede collective motion

Supplementary Figure 13(a) shows the distribution of angular velocities (calculated using the collective coordinate) from experiment in a filled ring trap that deviates from a single Gaussian shape. The bimodal probability distribution becomes more apparent at longer lag times, as seen in Supplementary Figure 13(b). The velocity distribution is fit to a two-Gaussian model for the lag time of  $\tau = 50$  ms (i.e., 10 frames). The first peak is centered at zero and the second near 100 deg/s. The velocity data are also shown for  $\tau = 5$  ms lag time (i.e., 1 frame). This distribution is mono-modal so only a single Gaussian is fit to the  $\tau = 5$  ms (blue) distribution. The peak at zero velocity in the  $\tau = 50$  ms lag time distribution results from instances in experiment when one or more particles in the ring become transiently stuck to or manifest high friction with the top glass cover slip; the sticking impedes the motion of the entire ring of nanoparticles. To illustrate this further, we eliminated frames with halted collective motion from our analysis and re-plotted the velocity distribution. The sticking-eliminated distributions for different lag times are shown in Supplementary Fig. 13(c). They are all centered near 100 deg/s angular velocity.



**Supplementary Figure 13: Stuck Particles in a Ring Trap.** (a) Experimental velocity distributions of a filled ring trap ( $R=6.2 \mu\text{m}$ ,  $N=65$ ) in RHC optical beam for different lag times  $\tau = 5$  ms, 10 ms, 25 ms and 50 ms. The associated time trajectories show instances of particles in the ring trap being stuck intermittently to the glass surface. (b) A two-Gaussian fit (red) and single Gaussian fit (blue solid curve) to the velocity distributions (open circles) for two lag times  $\tau = 50$  ms (10 frames; red) and  $\tau = 5$  ms (1 frame; blue), respectively. The red dashed vertical lines represent the means of the two-Gaussian fit. (c) Experimental velocity distributions of a filled ring trap ( $R=6.2 \mu\text{m}$ ,  $N=65$ ) in RHC light for different lag times  $\tau = 5$  ms, 10 ms, 25 ms and 50 ms after removing instances of particles in the ring trap being stuck intermittently to the glass surface.



## Supplementary Note 13. Autocorrelation function (ACF) analysis of the transport

Supplementary Figure 14(a) shows representative trajectories of the collective angular coordinate. For the case of experiments of a filled ring, we observe that there are periodic fluctuations in its trajectory between fast and slow motion ("run-pause" behavior; see Supplementary Fig. 15(a,b))—i.e., the motion of the ring is not of uniform speed.

We further quantify the transport of the ring of nanoparticles using the autocorrelation function (ACF) of the angular displacements of the collective coordinate. Supplementary Figure 14(b) shows the ACF of the collective angular displacement coordinate calculated using the MATLAB function [11]:

$$r_k = \frac{1}{c_0} \frac{1}{T} \sum_{t=1}^{T-k} (y_t - \bar{y})(y_{t+k} - \bar{y}) \quad (8)$$

where  $c_0$  is the sample variance of the time series,  $T$  is the total time (in frames),  $y$  is the angular displacement of the collective coordinate, and  $k$  is the lag time for which the autocorrelation function is calculated.

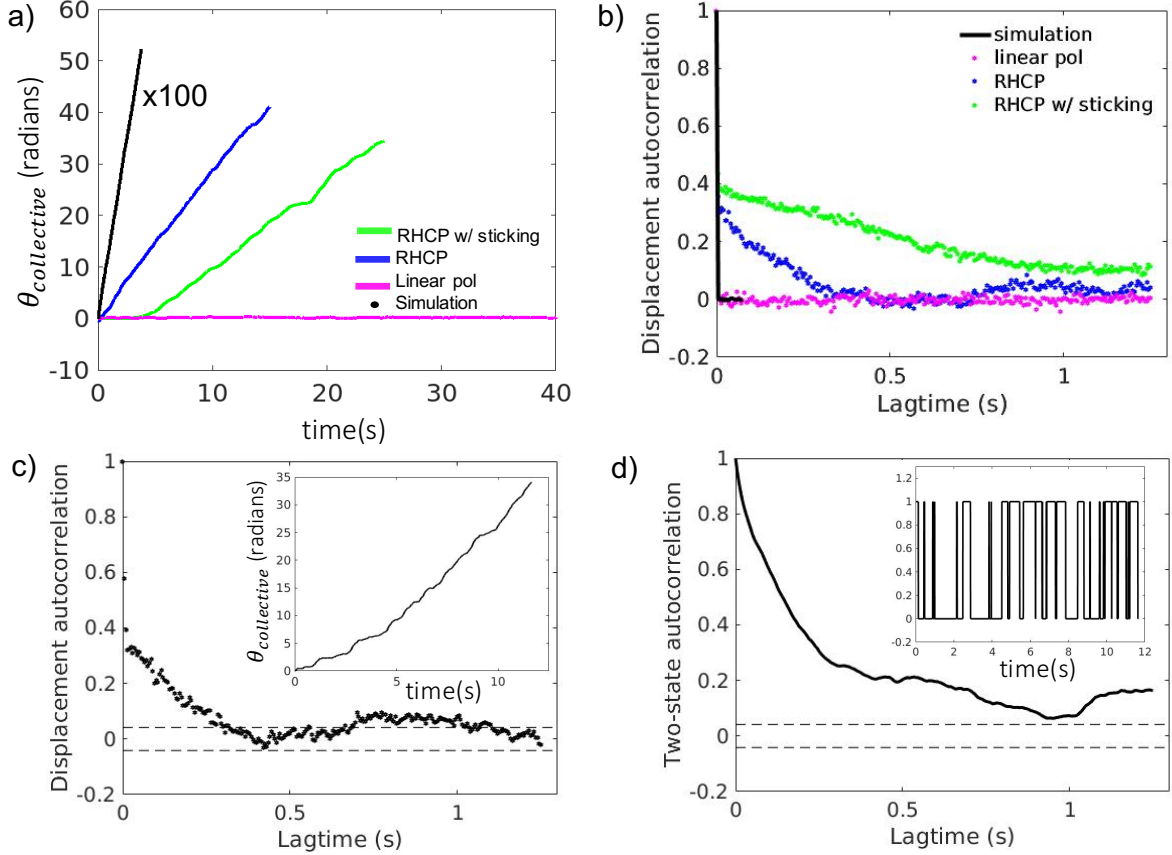
Supplementary Figure 14(b) shows that the ACF of nanoparticle angular displacement motion in optical ring traps decays extremely rapidly ( $\approx$  milliseconds) in experiments with linearly polarized light. This is because there is no driven motion of the ring of nanoparticles in the case of linearly polarized light and the motion of the Ag nanoparticles in the ring is simply uncorrelated random Brownian motion.

A similar very fast decay of the ACF (of the collective angular coordinate) occurs for a simulation of a filled ring of nanoparticles for RHC light. Even though there is strongly driven motion of the ring of nanoparticles in simulation, the ring is rotating with nearly constant velocity; i.e.,  $y_t \cong \bar{y}$ . Since we take the difference in the ACF calculation using Supplementary Eq. 8, therefore the ACF goes promptly to zero.

By contrast, Supplementary Fig. 14(b) also shows that the ACF of experimental data for a filled ring illuminated with circularly polarized light decays much more slowly. The decay time is even longer for the case where one or a few of the particles in the ring become transiently "stuck" to the top glass cover slip (see Supplementary Fig. 13). The "non-uniformity" of the motion of the ring results

in long timescale correlations between displacements, and hence a longer decay time of the ACF that is determined by the timescale of the motion of the ring of nanoparticles switching between fast and slow (stuck particle) velocities. These random "sticking" fluctuations are not included in the EDLD simulations and trajectories associated with Supplementary Fig. 14(b).

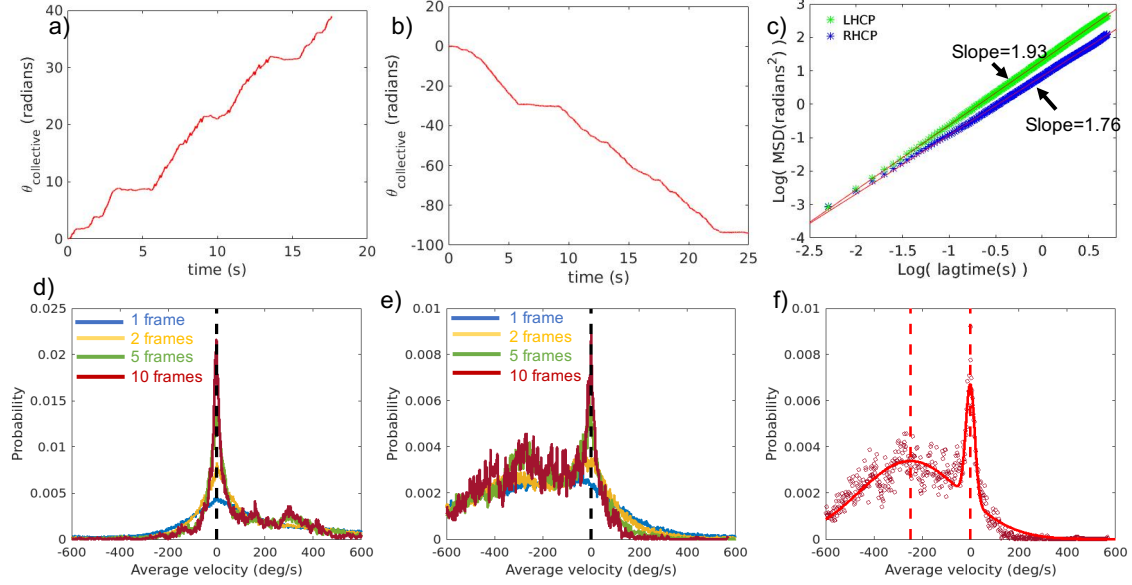
To demonstrate that the “run-pause” transport dynamics can cause long-time correlations, we choose an experimental video of the dynamics of a ring of nanoparticles where the speed of the ring changes drastically when there is a gap in the ring compared to when there is no gap in the ring (see Fig. 3 in the main text). The corresponding displacement ACF shown in Supplementary Fig. 14(c) decays slowly. The trajectory of the collective coordinate shown in the inset reflects the ring’s speed fluctuating between fast and slow modes of motion. We model this behavior with a simple two-state system: one state represents having a gap in the ring (corresponding to a value of 1) and the other state where there is no gap (corresponding to a value of 0). Supplementary Figure 14(d) shows that the corresponding ACF for this model decays similarly to the one in Supplementary Fig. 14(c). This correspondence demonstrates that the slower decay time of the experimental ACF for experiments with fluctuating interparticle separations arises from the switching of the motion of the ring of nanoparticles between slow and fast modes (i.e., “run-pause” behavior) that occurs on various timescales.



**Supplementary Figure 14: Angular displacement autocorrelation function (ACF) analysis of measured and simulated motion of rings of nanoparticles.** (a) The trajectories of the angular collective coordinate as a function of time for experimental and simulated rings of nanoparticles. Radius of the ring is  $4.1 \mu\text{m}$ . The experiments are with linearly polarized light and RHC polarized light; the latter with and without stuck particles. The simulation is with RHC light. The time scale of the simulation is much shorter than in experiment. Therefore, the simulated trajectory is magnified by 100x for visual convenience. Note the speed of rotation of the ring of nanoparticles in the simulation is greater than that in experiments. This is due to the lack of frictional drag with the charged glass surface in the simulations. This surface-associated friction slows the ring of nanoparticles in experiments. Simulations of the dynamics for the time scales of the experiments does not yield significantly different results. (b) The corresponding displacement ACF (of the collective angular coordinate) as a function of lag time. (c) The displacement ACF of the collective coordinate trajectory for a ring with a gap that opens and closes spontaneously. Inset shows the corresponding trajectory of the collective coordinate. (d) The displacement ACF of the model two-state system where the first state (value of 1) represents the ring with a gap and the second state (value of 0) represents the ring with no gap. The inset shows the state of the model system as a function of time.

## Supplementary Note 14. Non-uniform experimental velocity distributions

Figure 2(e-g) of the main text shows experimental trajectories of the ring of nanoparticles for LHC and RHC polarized incident light. Supplementary Figure 15 shows that the motion of the ring of nanoparticles is not uniform. Supplementary Figure 15(a,b) show the trajectory of the collective coordinate of the ring of nanoparticles over time for RHC and LHC polarized incident light, respectively. The trajectories show “run-pause” behavior, characterized by a “staircase” trend of the collective coordinate. However, the MSDs shown in Supplementary Figure 15(c) indicate driven transport for both RHC and LHC polarized incident light. Supplementary Figure 15(d,e) show the distribution of angular velocities (using individual nanoparticle trajectories and not the collective coordinate) for RHC and LHC polarized incident light, respectively. They show a peak centered at zero and an asymmetric tail at larger velocities. The asymmetric tail of the distributions correspond to the particles’ driven motion in a particular direction (“runs”) and the large peak centered at zero corresponds to their “pauses” at times during the trajectory. The velocity distributions are captured by a two-Gaussian fit. Supplementary Figure 15(f) shows a two-Gaussian fit to the velocity distribution for LHC polarized incident light. The peak of the first Gaussian is centered at zero and that of the second Gaussian at around -200 deg/s. There could be many factors contributing to the non-uniform motion of the ring, including mechanical friction, electrostatic interactions with the glass cover slip and a non-uniform intensity and phase profile of the ring trap (refer to Section 13 for additional details and discussion).

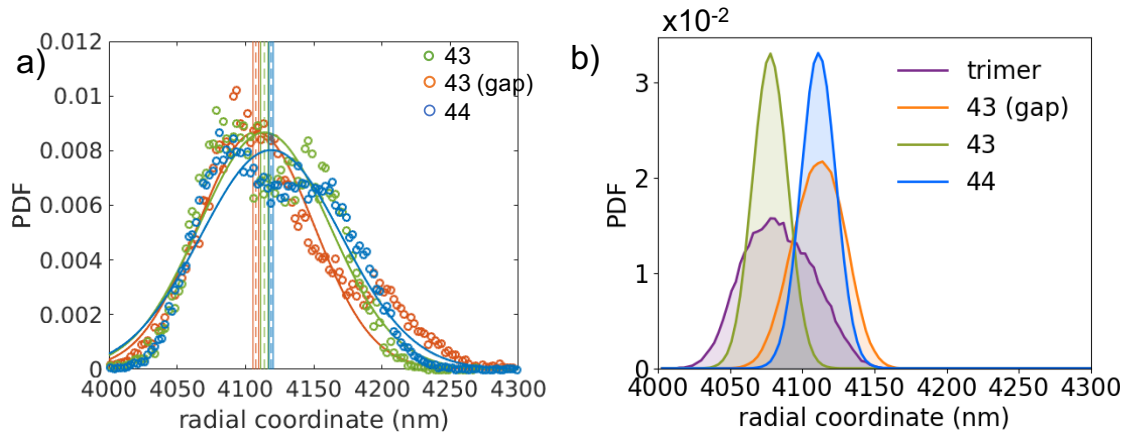


**Supplementary Figure 15: Sticking-perturbed nanoparticle velocity distributions still show strongly driven N-body forces and collective motion.** (a) The trajectory of the collective coordinate as a function of time for a ring of radius  $4.1 \mu\text{m}$  ( $N=44$ ) with RHC incident light. (b) The trajectory of the collective coordinate as a function of time for a ring of radius  $4.1 \mu\text{m}$  ( $N=44$ ) with LHC incident light. Note the "staircase" or "run-pause" type of behavior of the trajectories in (a,b). (c) The angular mean-squared displacements (MSDs) of the collective coordinate of the ring of nanoparticles as a function of  $\log(\text{lag time})$  with RHC-polarized light and LHC-polarized light. (d-e) The corresponding angular velocity distribution of individual nanoparticle trajectories and not the collective coordinate for (d) RHC-polarized light and (e) LHC-polarized light. Both the velocity distributions in (d) and (e) are plotted for different lag times,  $\tau = 5 \text{ ms}$  (1 frame),  $10 \text{ ms}$  (2 frames),  $25 \text{ ms}$  (5 frames) and  $50 \text{ ms}$  (10 frames). The asymmetric tail of the distributions indicate the particle's driven motion in a particular direction ("runs") and the large peak centered at zero corresponds to their "pauses" during the trajectory. (f) A two-Gaussian fit (red solid) to the velocity distribution (red circles) for LHC incident light for a lag time of  $50 \text{ ms}$  (10 frames). The red dashed vertical lines are the means extracted from the fit.

## Supplementary Note 15. Radial coordinate in a driven ring

Figure 3 of the main text shows how the N-body force varies as the interparticle separation in the ring changes when an extra particle (or gap) is added to the ring of nanoparticles. Supplementary Figure 16 shows how the radius of the ring trap changes as the extra particle (or gap) is added. Supplementary Figure 16(a) shows the experimental average radial distance and Supplementary Figure 16(b) the simulated average radial distance of the nanoparticles in a ring with 43 particles, 43 particles with a large gap in the ring, and a 44 particle fully filled ring (see Figure 3(a-c) of the main text). In simulation, the radius of the ring of particles increases when there is a gap (or 44 particles) relative to the radius in the case of 43 particles in order to accommodate the extra gap (particle). However, it is not as clear that the ring expansion occurs in experiment as it is obscured by the wider distribution of radial distances due to the lower optical power density in experiment. As such, the experimental mean radial distances for the three cases (dashed vertical lines) are not as significantly different from one another as they are in simulation.

Additionally, the radial position distributions shown in Supplementary Fig. 16(a) allow determines the stiffness coefficients,  $k_r$ , of the experimental optical trap in the radial direction. The radial stiffness coefficients are determined to be approximately 1.78 pN/ $\mu\text{m}$ , 1.79 pN/ $\mu\text{m}$ , 1.81 pN/ $\mu\text{m}$  for the cases of 44 particles, 43 particles, and 43 particles with gap, respectively.



**Supplementary Figure 16: Radial Coordinate in Driven Ring.** (a,b) Distribution of radial coordinate of particles in the ring in both (a) experiment and (b) simulation for a ring with 43 equally spaced particles, 43 particles with a gap, and fully filled ring with 44 particles. Colored solid curves are Gaussian fits to the distributions and colored dashed vertical lines indicate the means of the fit. Solid vertical lines are the 95% confidence intervals of the means. The experimental data are derived from Videos 4-6.

## Supplementary Note 16. Consideration of contributions to the N-body effect from nanoparticles' absorption

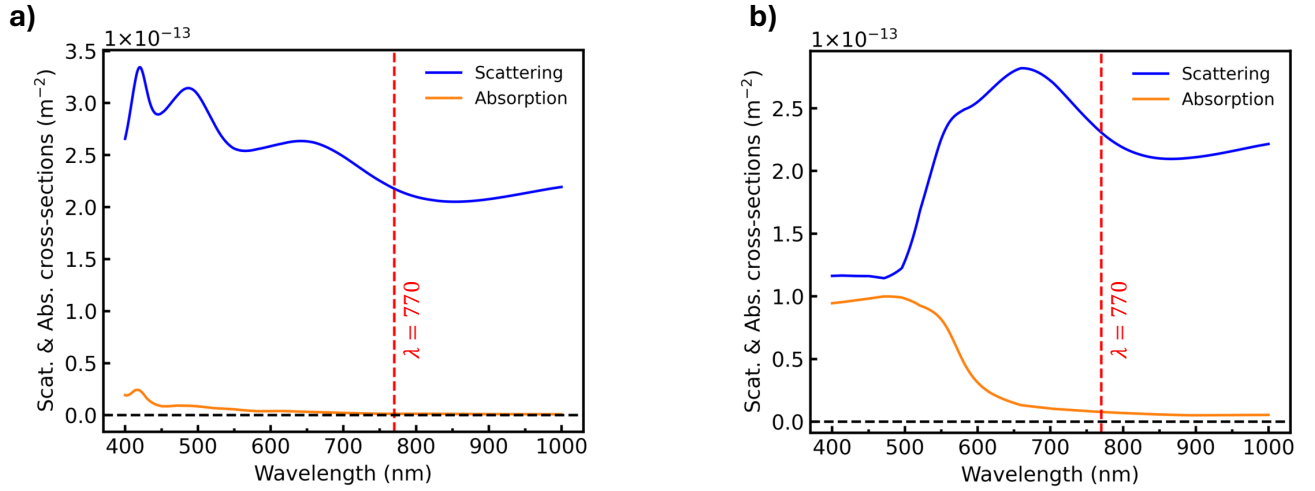
In a two-body system, the non-reciprocal optical forces rely on the differing polarizabilities ( $\alpha_1, \alpha_2$ ) of the constituent nanoparticles. Based on Aristide Dogariu's work [12], the non-reciprocal optical force is proportional to the polarizabilities, expressed as  $-\alpha_1' \alpha_2'' + \alpha_2' \alpha_1''$ . Here, the single and double prime symbols in the superscript denote the real and imaginary parts of the polarizabilities, respectively, with the letter featuring the absorbing property of matter. This proportionality explicitly demonstrates that a nonzero imaginary part of the polarizability (i.e., the nanoparticles' absorbing property) is necessary for generating non-reciprocal optical forces. However, it does not imply that the absorption of constituent nanoparticles must be intense. In fact, in most cases, the absorption is minor with limited contributions.

As shown in Supplementary Fig. 17, which shows the optical properties of the most commonly used nanoparticle materials (i.e., Ag and Au) in optical trapping studies, they both exhibit minimal absorption compared to their scattering strength when excited in their off-resonance spectral range. In our experiments, we chose a trapping laser wavelength of 770 nm, which is significantly distant from the dipolar resonance of a 150 nm dia. Ag nanoparticle. At this spectral position (indicated by the red vertical dashed line in Supplementary Fig. 17a), the Ag nanoparticle's absorption is nearly zero and thus negligible, indicating that its contribution to optical forces can be justifiably ignored in the N-body system proposed here.

Nevertheless, a strong absorbing property of nanoparticles could play a crucial role in N-body nonreciprocal interactions if the constituents were excited resonantly; however, this aspect is not considered in our current study due to the fact that the investigated Ag nanoparticles exhibit trivial absorption at the trapping laser wavelength.

Rather, the main source of the putative non-reciprocal force in the case of 2-nanoparticle OM systems is the phase shift of the scattered waves. Since the nanoparticles scatter light elastically, the resultant interference between the nanoparticle scattering can change the direction of the resulting wavefront.

Rather, the main source of the putative non-reciprocal force in the case of 2-nanoparticle OM systems is the phase shift of the scattered waves. Since the nanoparticles scatter light elastically, the resultant interference between the nanoparticle scattering can change the direction of the resulting wavefront. The argument is similar to wavefront construction using Huygens wavelets. These ideas were presented in our previous papers [13, 14].



**Supplementary Figure 17: Absorption properties of Ag and Au nanoparticles with a diameter of 150 nm.** (a) and (b) show the calculated scattering (blue curve) and absorption (orange curve) spectra of Ag and Au nanoparticles, respectively. The red and black dashed lines highlight the spectral location of the 770 nm trapping laser wavelength used in the experiment and the zero value, respectively.

## Supplementary References

1. He, H., Friese, M., Heckenberg, N. & Rubinsztein-Dunlop, H. Direct observation of transfer of angular momentum to absorptive particles from a laser beam with a phase singularity. *Physical review letters* **75**, 826 (1995).
2. Friese, M., Enger, J., Rubinsztein-Dunlop, H. & Heckenberg, N. R. Optical angular-momentum transfer to trapped absorbing particles. *Physical Review A* **54**, 1593 (1996).
3. Friese, M. E., Nieminen, T. A., Heckenberg, N. R. & Rubinsztein-Dunlop, H. Optical alignment and spinning of laser-trapped microscopic particles. *Nature* **394**, 348–350 (1998).
4. Friese, M., Rubinsztein-Dunlop, H., Gold, J., Hagberg, P. & Hanstorp, D. Optically driven micromachine elements. *Applied Physics Letters* **78**, 547–549 (2001).



5. Roichman, Y. & Grier, D. G. *Three-dimensional holographic ring traps* in *Complex Light and Optical Forces* **6483** (2007), 64830F.
6. Figliozzi, P. *et al.* Driven optical matter: Dynamics of electrodynamically coupled nanoparticles in an optical ring vortex. *Physical Review E* **95**, 022604 (2017).
7. Peterson, C. *et al.* Electrodynamic Interference and Induced Polarization in Nanoparticle-Based Optical Matter Arrays. *The Journal of Physical Chemistry C* **128**, 7560–7571 (2024).
8. Ashkin, A., Dziedzic, J. M., Bjorkholm, J. & Chu, S. Observation of a Single-Beam Gradient Force Optical Trap for Dielectric Particles. *Opt. Lett.* **11**, 288–290 (1986).
9. Pelton, M. *et al.* Optical trapping and alignment of single gold nanorods by using plasmon resonances. *Optics letters* **31**, 2075–2077 (2006).
10. Yan, Z., Sajjan, M. & Scherer, N. F. Fabrication of a material assembly of silver nanoparticles using the phase gradients of optical tweezers. *Phys. Rev. Lett.* **114**, 143901 (2015).
11. MATLAB. <https://www.mathworks.com/help/econ/autocorr.html>. Online; Accessed 2021-08-17.
12. Sukhov, S., Shalin, A., Haefner, D. & Dogariu, A. Actio et Reactio in Optical Binding. *Opt. Express* **23**, 247–252 (2015).
13. Yifat, Y. *et al.* Reactive optical matter: light-induced motility in electrodynamically asymmetric nanoscale scatterers. *Light: Science & Applications* **7**, 105 (2018).
14. Peterson, C. W., Parker, J., Rice, S. A. & Scherer, N. F. Controlling the Dynamics and Optical Binding of Nanoparticle Homodimers with Transverse Phase Gradients. *Nano Lett.* **19**, 897–903 (2019).